



# New insights into the early opening of the Equatorial Atlantic Gateway revealed through a magneto-cyclostratigraphy framework from the Brazilian Equatorial Margin



J. M. F. Ramos <sup>1,2</sup>, J. F. Savian <sup>1,3</sup>, D. R. Franco <sup>4</sup>, M. F. Figueiredo <sup>5</sup>, C. A. Pontel <sup>1</sup>, J. N. L. Lacerda <sup>1</sup>, J. Kuchle <sup>3</sup>, P. A. Souza <sup>3</sup> & R. P. Silva Jr <sup>5</sup>

The opening of the Equatorial Atlantic Gateway reshaped Earth's ocean–atmosphere system. Rifting between South America and Africa drove a shift from continental–lacustrine to evaporitic and eventually marine environments, though the timing and duration of these transitions remain debated. Here we present a high-resolution magneto–cyclostratigraphic age model from the São Luís–Grajaú Basin (Brazilian Equatorial Margin), based on two geomagnetic reversals and Milankovitch-band cycles, yielding a 405-kyr astronomically tuned timescale. This framework enables: (i) correlation of Tethyan events with the first marine incursion in the Brazilian margin at 117.2 Ma; (ii) precise dating of the M-1r subchron at  $116.93 \pm 0.14$  Ma and subchron “2” at  $116.28 \pm 0.14$  Ma; and (iii) constraint of Equatorial Belt humidification onset to  $\sim 116.4$  Ma,  $\sim 800$  kyr after the marine incursion. These results provide a robust chronostratigraphic reference for the early equatorial Atlantic opening and inform Aptian paleoclimate responses during Gondwana breakup.

Deciphering the tectonic evolution of the Equatorial Atlantic Gateway (EAG)—a driver of profound changes in ocean circulation, deep-ocean oxygenation, carbon cycling, and Aptian paleoclimate—is pivotal for understanding global oceanographic and tectonic evolution. Its evolution has far-reaching implications for water-mass exchange among late Mesozoic basins and for kinematic models of Gondwana breakup and passive margin development<sup>1,2</sup>. In its initial stages, the EAG consisted of still narrow and poorly connected, steep-sided *pull-apart* basins, with limited ventilation<sup>3–6</sup>. During the early stages of the supercontinent breakup the continental systems gradually changed to mixed, transitional, and eventually fully marine depositional environments, including evaporitic phases<sup>2,4,7,8</sup>.

Marine incursions over lacustrine and continental environments were likely sporadic and linked to mid-Cretaceous sea-level rise<sup>9</sup>, potentially entering through the Guinea Passage<sup>2</sup>. Nd-isotope records indicate that

these earliest incursions lacked significant far-field water-mass exchange<sup>10</sup>. These incursions are thought to have occurred between the Barremian and Albian stages ( $\sim 126.5$ – $113$  Ma)<sup>1–7,10,11</sup>, coinciding with abrupt climate events and Oceanic Anoxic Events (OAEs) that disrupted the greenhouse climate of the Cretaceous, affecting global temperatures, seawater chemistry, and oxygen levels<sup>10,12,13</sup>. However, the timing of the initial marine incursions remains poorly constrained, as kinematic models detailing the early opening history of the Equatorial Atlantic are not yet fully developed<sup>1,2</sup>.

During the Cretaceous Normal Polarity Superchron (CNPS), the geomagnetic field predominantly exhibited normal polarity. However, constraints imposed by deep-tow magnetic surveys continue to limit tectonic reconstructions for this period<sup>14,15</sup>. Consequently, kinematic models often depend on interpolations, complicating efforts to more precisely constrain the relative motions between South America and Africa<sup>1,2</sup>. While rapid geomagnetic polarity reversals—such as the ISEA and ‘2’ subchrons—

<sup>1</sup>Programa de Pós-Graduação em Geociências, Universidade Federal do Rio Grande do Sul, Porto Alegre, RS, Brazil. <sup>2</sup>Petrobras Petróleo Brasileiro S.A. Av, Rio de Janeiro, RJ, Brazil. <sup>3</sup>Instituto de Geociências, Universidade Federal do Rio Grande do Sul, Porto Alegre, RS, Brazil. <sup>4</sup>Coordenação de Geofísica, Observatório Nacional, Rio de Janeiro, RJ, Brazil. <sup>5</sup>Centro de Pesquisas e Desenvolvimento Leopoldo Américo Miguez de Mello, Petrobras Petróleo Brasileiro S.A, Rio de Janeiro, Brazil. e-mail: [j.m.f.ramos@petrobras.com.br](mailto:j.m.f.ramos@petrobras.com.br)

have been documented and dated in other regions during the CNPS<sup>16–18</sup>, they remain undetected in the Equatorial Atlantic<sup>19</sup>.

Previous models have suggested that the EAG remained closed until the onset of the Albian (~113 Ma), when shallow-water exchange with the Tethys Ocean commenced<sup>1,19</sup>. However, more recent evidence indicates that the opening of the EAG began earlier, initiating a phase of limited—but nevertheless present—water exchange<sup>2,10,20</sup>. Notably, many studies converge on the Aptian stage as a critical period for this process<sup>2–7,10,20</sup>. Supporting this interpretation is the occurrence of Aptian planktonic foraminifera with Tethyan affinities<sup>20,21</sup>.

In the Tethyan Ocean, the upper Aptian is characterized by an atypical paleoclimatic phase known as the “cold snap,” a mid-Cretaceous cooling interval that disrupted the previously warm and equable climate conditions<sup>13</sup>. This event, involving a ~5 °C temperature decrease over ~2.4 Myr<sup>22</sup>, has been linked to enhanced oceanic crust production and the opening of the Atlantic Ocean<sup>10</sup>. Its signature is preserved in sea-surface temperature (SST) records and positive  $\delta^{13}\text{C}$  excursions, associated with biotic crises, the widespread collapse of oceanic stratification, and severe declines in planktonic foraminifera and nannoconid phytoplankton<sup>12</sup>. In the equatorial realm, the opening of the EAG and the mid-Cretaceous cold snap were closely tied to a latitudinal displacement of the proto-Intertropical Convergence Zone (ITCZ) and to consequent changes in precipitation regimes through the development of the Equatorial Humid Belt (EHB)<sup>7</sup>.

An integrated analysis of geological records from the Tethyan and Equatorial Atlantic realms provides a comprehensive view of paleoceanographic variability during the Aptian–Albian stages. In this framework, magneto-cyclostratigraphy stands out as a powerful approach, enabling

high-resolution correlations between distant regions. Resolving events at geological timescale resolution is essential to test potential causal links among the opening of the South and Equatorial Atlantic Oceans, the onset of the Aptian Cold Snap, and the breakdown of arid conditions across Gondwana<sup>7,8</sup>. Achieving this goal, however, hinges on the establishment of a robust age model for the Equatorial Atlantic that captures the earliest phases of its opening.

The Gondwana rifting process that ultimately led to the opening of the Equatorial Atlantic Ocean promoted the formation of sedimentary basins along the Brazilian Equatorial Margin (BEM)<sup>2–6,19</sup>. Sedimentary archives from the BEM, Fig. 1, provide crucial insights into the initial opening of the proto-Equatorial Atlantic Ocean and the evolution of the EAG. The observed succession of facies and depositional systems in the BEM is consistent with the infilling patterns expected for *pull-apart* basins<sup>4–6,8,23</sup>. Therefore, examining the continental-to-marine sedimentary transitions preserved in basins formed during the BEM rifting and *sag* phases is key to reconstructing the paleoclimatic responses to these major tectonic and oceanographic events.

The BEM is defined by three major east–west-trending oceanic fracture zones—St. Paul, Romanche, and Chain—that separate distinct margin segments and reflect the influence of dextral strike-slip plate motion, forming a series of oblique structural steps<sup>1,2,5,19</sup>. This region is classified as an oblique margin, where transform faults segment *pull-apart* sedimentary basins<sup>6,10</sup> resulting from seafloor spreading propagating northward into the Equatorial Atlantic Ocean. The São Luís–Grajaú Basin, located in northern–northeastern Brazil, is one of the sedimentary basins shaped predominantly by transtensive tectonics during the Aptian and Albian stages<sup>3–6</sup>. Geochronological issues in the São Luís–Grajaú Basin include the

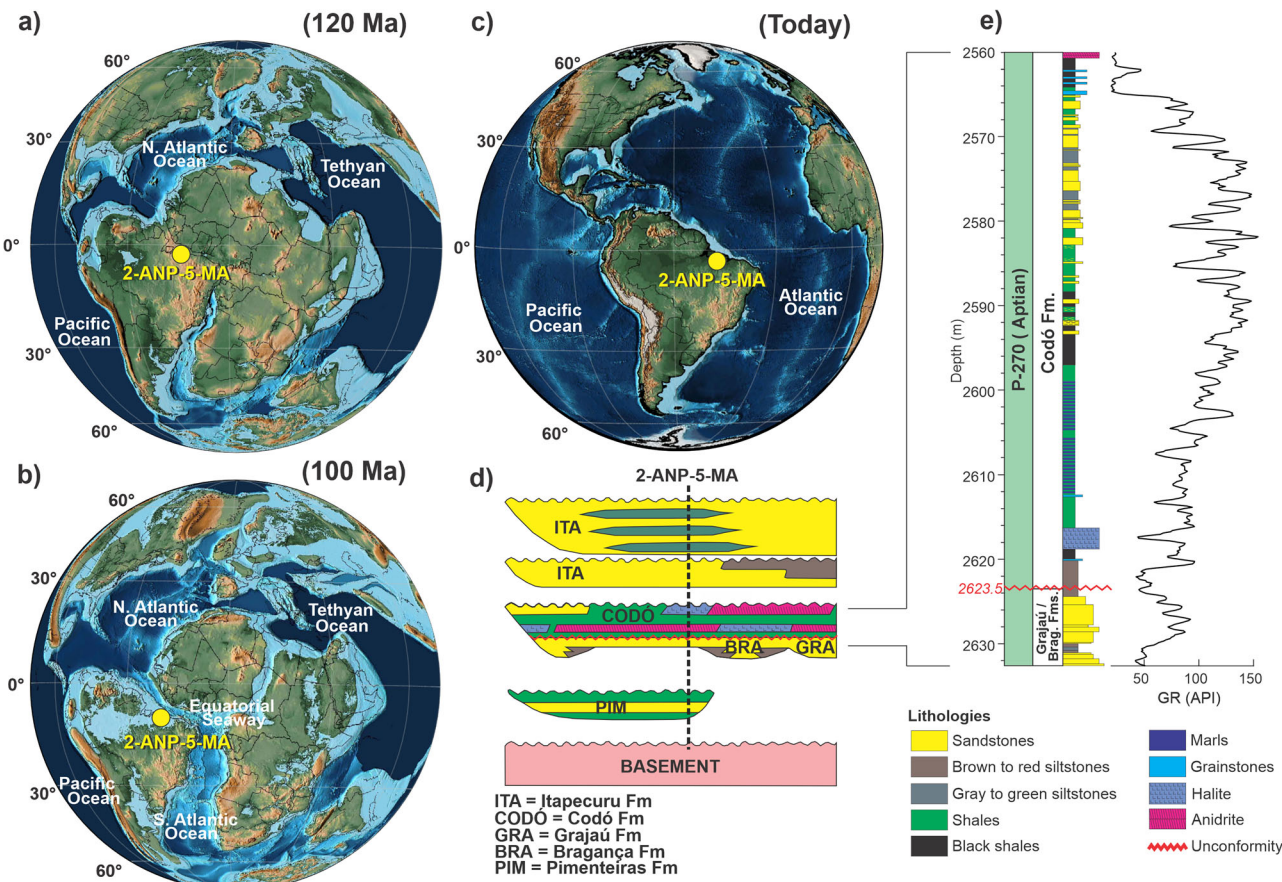


**Fig. 1 | Paleoreconstruction maps during the Cretaceous.** **a** 120 and **b** 100 Ma, with the position of 2-ANP-5-MA core (generated with Gplates software; Müller et al.<sup>60</sup>). **c** Present day position of the 2-ANP-5-MA core. **d** São Luís Basin

chronostratigraphic chart with the approximate location of the studied core plotted (Gonzalez et al.<sup>8</sup> & Zalán<sup>6</sup>). **e** Lithostratigraphic scheme of the studied portion (lower Codó Fm) of the 2-ANP-5-MA core with the gamma-ray log.

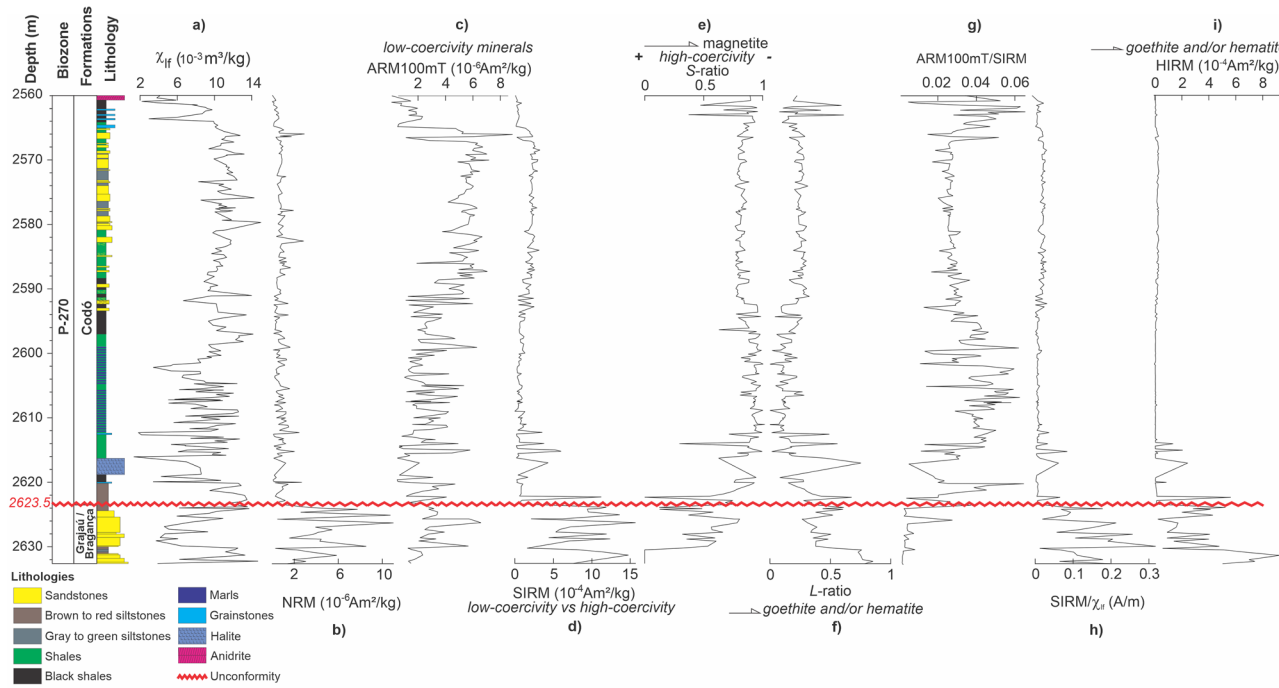


**Fig. 2 | Rock magnetic parameters of the studied interval of the 2-ANP-5-MA core.** **a** Low-field ( $\chi_{lf}$ ) magnetic susceptibility. **b** Natural remanent magnetization (NRM). **c** Anhysteretic remanent magnetization at 100 mT ( $ARM_{100mT}$ ).

**d** Saturation isothermal remanent magnetization (SIRM). **e** S-ratio. **f** L-ratio. **g** Ratio between ARM at 100 mT and SIRM. **h** Ratio between SIRM and  $\chi_{lf}$ . **i** Hard isothermal remanent magnetism (HIRM).

timing of the Equatorial Atlantic Ocean's opening, the formation of main basins, and the ages of hydrocarbon source rocks.

However, constraining the age of these sediments remains difficult owing to the paleogeographic setting of Gondwana's initial breakup, which was dominated by lacustrine and fluvial environments with only sporadic marine incursions<sup>3–7</sup>—conditions that typically lack planktonic foraminiferal bioevents or calcareous nannofossils capable of providing reliable age constraints or duration estimates. Furthermore, the presence of unconformities, which are common in coastal/proximal environments, presents an additional challenge in refining chronostratigraphy.

The timing of the EAG opening varies between 140–92 Ma<sup>1,9,14,19,24</sup>. However, the concept of “Open Ocean” remains problematic among these publications, as the exact definition of the term “opening” for the proposed ages is usually not specified: whether it refers to the moment when the oceanic ridge forms; the first episodic or temporary incursions of seawater into previously non-marine areas; or the establishment of fully marine (deep-water) conditions. Although oceanic ridges developed within enclosed basins separated by fracture zones in the EAG—with such features present near the BEM since the Jurassic<sup>24</sup>—the term “opening” generally refers to the interval between 125 and 112 Ma<sup>20</sup>, 126–120 Ma<sup>19</sup>, 100 Ma<sup>1</sup> and 108–92 Ma<sup>15</sup>. Recent evidence indicates that this event may have initiated as early as the Barremian–Aptian transition (120.2 Ma)<sup>22,25</sup>. Additionally, the *Calpionellopsis oblonga* bioevent in the Romanche Fracture Zone, dated to 140 Ma<sup>11</sup>, suggests that marine ingress occurred at least 40 million years before the first ridge was established. In this study, we adopt the definition of seawater incursion proposed by Cui et al.<sup>26</sup> as the “initial lacustrine–marine transition, in which seawater flows into a restricted lacustrine basin via meandering channels, overflow, or seepage across geographic barriers”.

This study presents a chronostratigraphic refinement of the timing of the earliest marine incursions in the BEM, based on analysis of the 2-ANP-5-MA core from the São Luís–Grajaú Basin, where marine conditions are evidenced by the occurrence of fish, mollusks, dinoflagellate cysts, planktonic foraminifera and  $C_{30}$  regular sterane<sup>7,8,20,21</sup>. By integrating magnetostratigraphy and cyclostratigraphy, an age model was developed for the studied section, offering new insights into the timing of the Gondwana rift process that led to lacustrine-to-marine transition. Our results provide a

robust chronostratigraphic reference for the opening of the Equatorial Atlantic, with far-reaching implications for Aptian paleoclimate dynamics and for synchronous geological events across the Tethys Ocean and proto-Equatorial Atlantic.

## Results and discussions

### Rock magnetism properties of the 2-ANP-5-MA core sediments

The 2-ANP-5-MA drill site (lat.  $2^{\circ}14'45.32''$  N; long.  $45^{\circ}54'54.32''$  E) is located within the São Luís–Grajaú Basin and recovered 2914 m of core comprising diverse lithologies (Fig. 1). From the top down to 2469 m, sandstones of the Itapecuru Fm. were sampled, transitioning through the Codó Fm. and reaching a unconformity (Alagoas unconformity) at 2630 m that separates it from the underlying Grajaú/Bragança Fm. (Fig. 1). The Codó Fm. is characterized by thick shale layers interbedded with evaporitic, carbonate, and siliciclastic facies<sup>3,7,8</sup> and is associated with the P-270 biozone (*Sergipea variterrucata*), related to the late Aptian<sup>7,8,27,28</sup>.

Low-field magnetic susceptibility ( $\chi_{lf}$ ), which serves as an environmental and paleoclimatic proxy for magnetic mineral concentration, displays a nearly sinusoidal pattern with an approximate wavelength of 60 m (Fig. 2a and Supplementary Data 1). The lower half of the studied interval (until 2623.5 m) shows greater variations in  $\chi_{lf}$  (ranging from 2 to  $14 \times 10^{-3} \text{ m}^3/\text{kg}$ ), while the upper half (2623.5–2650 m) displays a less noisy pattern with a mean value of  $11 \times 10^{-3} \text{ m}^3/\text{kg}$ . The natural remanent remagnetization (NRM) along the sampled section of the Grajaú/Bragança Fm. ranges from 1 to  $10 \times 10^{-6} \text{ Am}^2/\text{kg}$  (Fig. 2b). Below 2623.5 m, the values drop sharply and remain roughly constant ( $\sim 1 \times 10^{-6} \text{ Am}^2/\text{kg}$ ) throughout the Codó Fm. (Fig. 2b), indicating a significant change in dominant magnetic minerals, lithological, diagenetic, and/or thermal conditions between these two units.

The anhysteretic remanent magnetization 100 mT ( $ARM_{100mT}$ ) data allow the studied interval to be divided into three sections shown in Fig. 2c: the first, from the base of the studied interval up to 2590 m, oscillating with a constant trend and an average value of  $2 \times 10^{-6} \text{ Am}^2/\text{kg}$ ; the second, characterized by a plateau of higher values around  $6 \times 10^{-6} \text{ Am}^2/\text{kg}$ ; and the third interval, where  $ARM_{100mT}$  drops sharply from 2565 m to values around  $1 \times 10^{-6} \text{ Am}^2/\text{kg}$  (Fig. 2c). The saturation isothermal remanent

magnetization (SIRM) profile (Fig. 2d) shows a similar behavior to the NRM profile (Fig. 2a), suggesting a sharp change in magnetic mineralogy. The lower portion, Grajaú/Bragança Fm., exhibits average SIRM values of  $10 \times 10^{-4}$  Am<sup>2</sup>/kg, indicating the presence of high-coercivity magnetic minerals. In contrast, the Codó Fm. shows low and constant values (around  $1 \times 10^{-4}$  Am<sup>2</sup>/kg), indicating the predominance of low-coercivity magnetic minerals (Fig. 2d).

The S-ratio profile (Fig. 2e), reinforces the information from the SIRM, suggesting high coercivities for the magnetic minerals of the Grajaú/Bragança Fm. compared to the Codó Fm. The Codó Fm. shows high S-ratio values (near 1), indicating that magnetite is likely the dominant magnetic mineral. Only the top five meters of the Codó Fm. exhibit intermediate S-ratio values, suggesting a mixture of magnetic minerals. From the base to the top of the studied section, there is a noticeable decrease in L-ratio profile values (Fig. 2f). The highest values (reaching 0.8) are found in the lower three meters. From this point, there is a sharp decrease to 0.5, which then gradually reduces further until reaching a minimum plateau, from the halite to the top of the black shale. In the upper three meters of the studied section, the L-ratio values increase again to around 0.5.

The Grajaú/Bragança Fm. exhibits the lowest values of  $\text{ARM}_{100\text{mT}}/\text{SIRM}$  ( $\sim 0.01$ ), which gradually increase from the base of the Codó Fm. up to the 2608 m mark (Fig. 2g). Fluctuations are observed in the heterolithic interval composed of grainstones and shales, with a decrease back to values of 0.02 at 2565 m depth. The SIRM/χ<sub>lf</sub> ratio provides an estimate of magnetic grain size variations<sup>29,30</sup>. Excluding the Grajaú/Bragança Fm., where values range from 0.1 to 0.3 A/m, the rest of the studied interval is nearly constant, with values close to zero (Fig. 2h).

Changes in hard isothermal remanent magnetization (HIRM) indicate variations in the absolute concentration of hematite and/or goethite when the L-ratio remains relatively constant, as it excludes the contributions of strongly magnetic, low-coercivity ferrimagnetic minerals, which saturate magnetically at fields below 300 mT<sup>31</sup>. Despite occasional instances in the Codó Fm. with values around  $2 \times 10^{-4}$  Am<sup>2</sup>/kg, the HIRM profile values (Fig. 2i) generally remain close to zero reflect the previously mentioned observations, which demonstrate the consistency of the magnetic mineralogy in the Codó Fm., in contrast to the Grajaú/Bragança Fm., which shows HIRM values reaching  $8 \times 10^{-4}$  Am<sup>2</sup>/kg.

Magnetic characterization reveals that most samples are dominated by low-coercivity magnetite, while others show significant contributions from hematite or superparamagnetic grains. Variations in hysteresis loops, IRM acquisition, and FORC diagrams indicate diverse magnetic mineral assemblages and domain states, ranging from single to pseudo-single domain (SD-PSD) behavior, likely reflecting different sedimentary and diagenetic histories<sup>32–35</sup>. Decomposition of IRM curves using Max UnMix suggests mixtures of magnetic populations with varying coercivities. Thermomagnetic analyses confirm magnetite and titanomagnetite as the primary magnetic carriers, with evidence of irreversible mineralogical transformations such as magnetite oxidation and pyrrhotite alteration<sup>36–39</sup>. Full hysteresis, IRM, FORC, and thermomagnetic data are provided in Supplementary Figs. S1–S3 and Supplementary Tables S1, S2.

## Magnetostratigraphy

All 254 specimens could be demagnetized by alternating field and thermal treatment showing stable characteristic remanent magnetization (ChRM) (Fig. 3a–f and Supplementary Data 2). Specimens that displayed reverse inclination (Fig. 3a), as well as those not fully demagnetized by alternating field treatment (Fig. 3e) were subsequently subjected to thermal demagnetization (Fig. 3b, f) on top of their 'twin' specimens. Supplementary Figs. S4–S7 present complementary data comprising vector end-point demagnetization diagrams, stereographic projections, and demagnetization intensity curves.

The P-270 biozone is assigned to with the late Aptian<sup>27,28</sup>, and the predominantly normal geomagnetic polarity observed through demagnetization analyses is consistent with the CNPS interval<sup>14,17–19</sup> (Fig. 4a). The median destructive field (MDF) – a proxy for the average coercivity of the

magnetic minerals present – has an average value of 23 mT for the entire interval of the Codó Fm., increasing to average values above 60 mT below the unconformity that separates it from the Grajaú/Bragança Fm., highlighting a change in the relative magnetic grain-size variation (Fig. 4b). Most of the samples present normal polarity (Fig. 4c). The mean inclination of the samples is  $-4.25^\circ$ , ranging from  $0^\circ$  to  $-15^\circ$  (Fig. 4c).

Specimens with inclination values greater than  $-15^\circ$  are likely associated with magnetic excursions and/or reversals. Therefore, three or more samples with positive inclinations and low angles (less than  $15^\circ$ ) are considered to characterize reverse intervals. Three intervals with reverse polarity were identified within the Codó Fm. Two of these, located between 2593.90–2594.91 m and 2614.54–2615.56 m, are considered reliable and are shown in Fig. 4c. A third reversed interval was observed at the base of the Codó Fm. (2621.78–2622.49 m); however, it was excluded from interpretation due to its proximity to the unconformity. This lower interval may reflect either iron remobilization or the influence of steeply dipping layers near the unconformity, which can compromise the reliability of the magnetic signal. Additionally, at the top of the studied interval, another reverse interval (with 3 samples) was discarded due to the high inclination angles (reaching up to  $45^\circ$ ). The Maximum Angular Deviation (MAD) of the alternating field demagnetization remained below  $10^\circ$ , with a mean MAD of  $3^\circ$ , which confirms the high quality of the ChRM directions. The samples thermally demagnetized (THD) have a MAD of less than  $15^\circ$ , with an average of  $6^\circ$  (Fig. 4d). Based on these results, we can affirm that the Codó Fm. is fully contained within the CNPS, where two short geomagnetic reversals are present (Fig. 4e).

## Cyclostratigraphy

The  $2\pi$ -MTM-Classic-AR(1) spectral analyses of χ<sub>lf</sub> data (after LOWESS detrending, 35% window) revealed a broad spectral content, frequently exceeding the 95–99.9% confidence levels (Fig. 5a, b). The continuity of these signals throughout the studied interval must be envisioned through the eFFT spectra for χ<sub>lf</sub> data and allowed us to distinguish four sets of low-frequency bands, common to both datasets and persistent throughout all studied interval: (i)  $1/0.05$ – $1/0.14$  m<sup>-1</sup> (central frequency of  $\sim 1/0.10$  m<sup>-1</sup>); (ii)  $1/0.22$ – $1/0.50$  m<sup>-1</sup>; and (iii)  $1/0.55$ – $1/0.90$  m<sup>-1</sup>; and (iv)  $1/1.0$ – $1/1.4$  m<sup>-1</sup> (highlighted rectangles in pale red, blue, orange, and pink, respectively, Fig. 5c). The observed wavelength ratios verified for the χ<sub>lf</sub> spectra ( $9.9, 3.3, 2.2, 0.94 = 10.53, 3.51, 2.34, 1$ ) are strikingly consistent with the expected for the Milankovitch spectral peak ratios for the top of Aptian stage (~116 Ma): ( $1/405, 1/125, 1/95, 1/38.7 = 10.46, 3.22, 2.45, 1$ )<sup>40</sup>.

Such findings lead us to assume that χ<sub>lf</sub> dataset evidenced the record of orbitally-paced variations of the 405-kyr long eccentricity (g<sub>2</sub>–g<sub>5</sub>), the 125–95-kyr short eccentricities (g<sub>4</sub>–g<sub>2</sub> and g<sub>4</sub>–g<sub>5</sub>, respectively) and the obliquities ( $\sim 51$ -kyr (p + s<sub>6</sub>),  $\sim 38$ -kyr (p + s<sub>3</sub>),  $\sim 29$ -kyr (p + s<sub>2</sub>)). The relatively low sampling resolution (~0.27 m), when compared to the estimated sedimentation rates, likely hindered the detection of precession-related frequency bands.

Cyclostratigraphic analyses combined with COCO/eCOCO Monte Carlo simulations (2000 iterations), indicate a most probable bulk sedimentation rate of  $\sim 3.2$  cm/kyr, with high statistical significance ( $p = 0.003$ ) and seven contributing orbital parameters. Despite a moderate correlation coefficient (0.329), this rate provides the best compromise between eCOCO and H<sub>0</sub> significance, as well as the greatest stratigraphic continuity in core 2-ANP-5-MA. Variations inferred from eCOCO and eH<sub>0</sub>SL suggest that sedimentation rates generally remained between 3 and 4.5 cm/kyr throughout most of the studied interval (Fig. 5d and Supplementary Fig. S8).

An age model was constructed by correlating the 405-kyr component filtered from the χ<sub>lf</sub> dataset with the 405-kyr long-eccentricity component from the La2004 astronomical solution<sup>41</sup> (Fig. 6). Using the ISEA subchron age<sup>18</sup> as an anchor, the long-eccentricity minimum between cycles E10 and E11 of the 405-kyr filtered χ<sub>lf</sub> signal was tuned to align in phase with the 405-kyr components of Laskar's astronomical solutions (Fig. 6 and Supplementary Figs. S8 and S9).

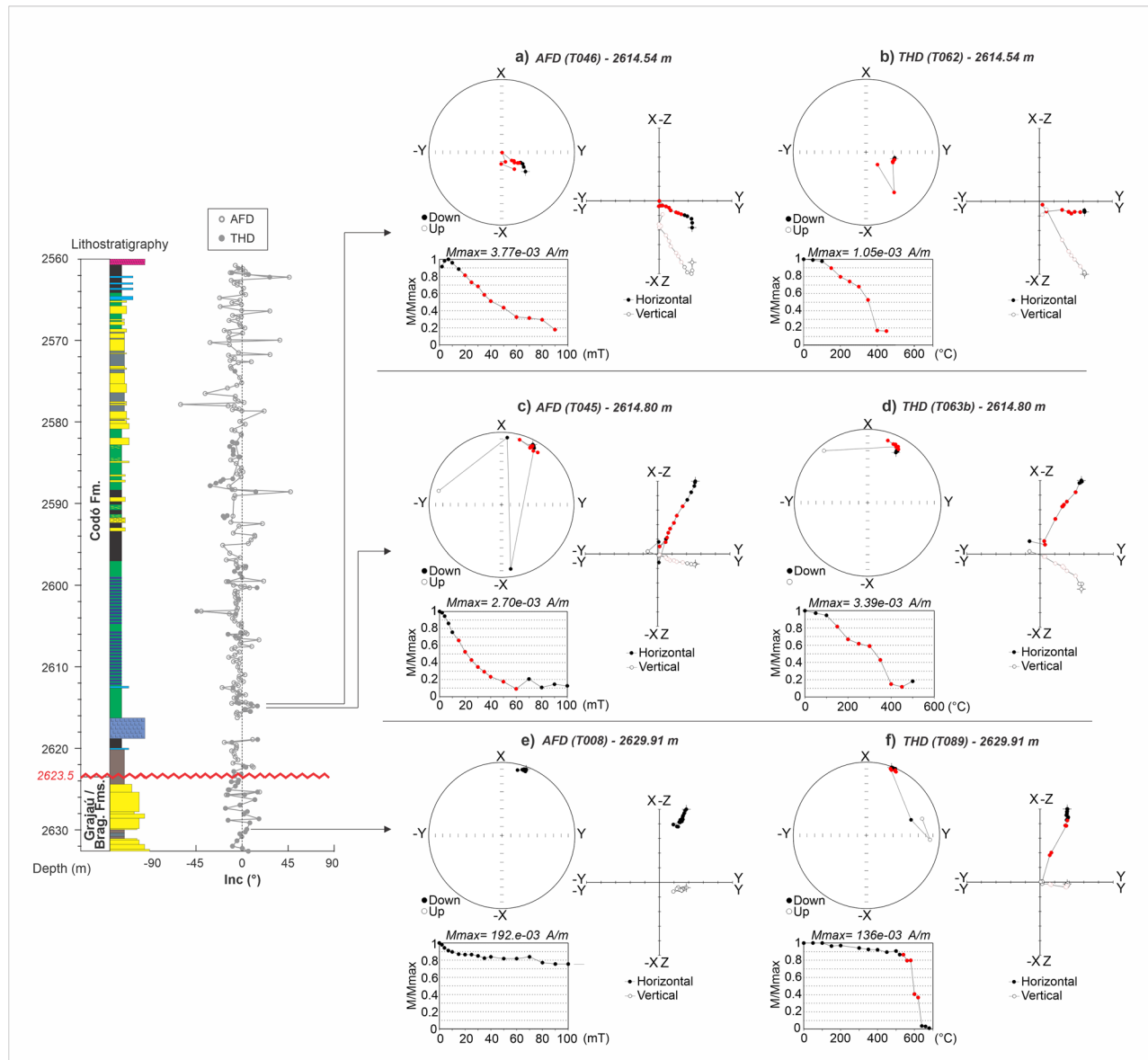


**Fig. 3 | Representative Vector end-point demagnetization diagrams, stereographic projections, and demagnetization intensity curves of representative samples from the 2-ANP-5-MA core. **a**** Alternate field demagnetization of the T046 (2614.54 m) sample. **b** Thermal demagnetization of the T046 (2614.54 m) sample.

**c** Alternate field demagnetization of the T045 (2614.80 m) sample. **d** Thermal demagnetization of the T045 (2614.80 m) sample. **e** Alternate field demagnetization of the T008 (2629.91 m) sample. **f** Thermal demagnetization of the T008 (2629.91 m) sample.

Anchoring the ISEA at 117.03 Ma<sup>18</sup> yielded a sedimentation accumulation rate (SAR) of ~3–4.5 cm/kyr. Because our tiepoint relies on the ages obtained by Ramos et al.<sup>18</sup>, which were based on the La2004 solution<sup>41</sup>, we also referenced the ages in this study to La2004. This approach allows a direct comparison of the ages and durations of the M-1r and '2' subchrons across different regions of the globe, derived from multiple proxies (Supplementary Fig. S10 and Supplementary Table S3).

Following the La2004 solution<sup>18,41</sup>, the remaining 405-kyr components were used to estimate an age uncertainty of 140 kyr, corresponding to the phase lag between La2004 and La2010c. A comparison of the age differences and timespans is presented in Supplementary Table S3. Despite the lower temporal resolution at DSDP Site 402A, previously defined chron durations fall within the assigned error range. Our floating astronomical timescale (FATS) - which comprises the interval of 2560.0 m to 2623.5 m of the 2-ANP-5-MA core - evidenced four long-eccentricity cycles, implying in a timespan of ~1.92 Myr (115.30–117.22 Ma). Furthermore, it was also possible to suggest new time spans for important geological

events recorded throughout the studied interval: 117.05 and 116.96 Ma for the base and the top of the halite, respectively; 116.94 and 116.91 Ma for the base and the top of the lowest reversal interval (interpreted here as the ISEA, or M-1r Chron); 116.36 Ma for the base of the lowest black shale; 116.30 Ma and 116.27 Ma for the base and the top of the upper geomagnetic reversal (interpreted here as the "2" Chron<sup>18</sup>; and 115.35 Ma for the base of the anidrite (Fig. 6).

#### Ephemeral reversed polarity episodes interrupting the CNPS

The CNPS (C34n Chron) spans ~38 Ma, from the early Aptian to the middle Santonian, with a predominantly stable magnetic field in normal polarity<sup>4,42</sup>. Although short-lived reversed polarity intervals have been documented within the CNPS<sup>17,18</sup> (Fig. 7), their brief duration, combined with limitations in sampling resolution (e.g., core spacing) and deep-tow survey coverage, makes them difficult to detect consistently. Consequently, the limited recognition of these abrupt magnetic fluctuations hampers their use as reliable tie points for kinematic reconstructions.

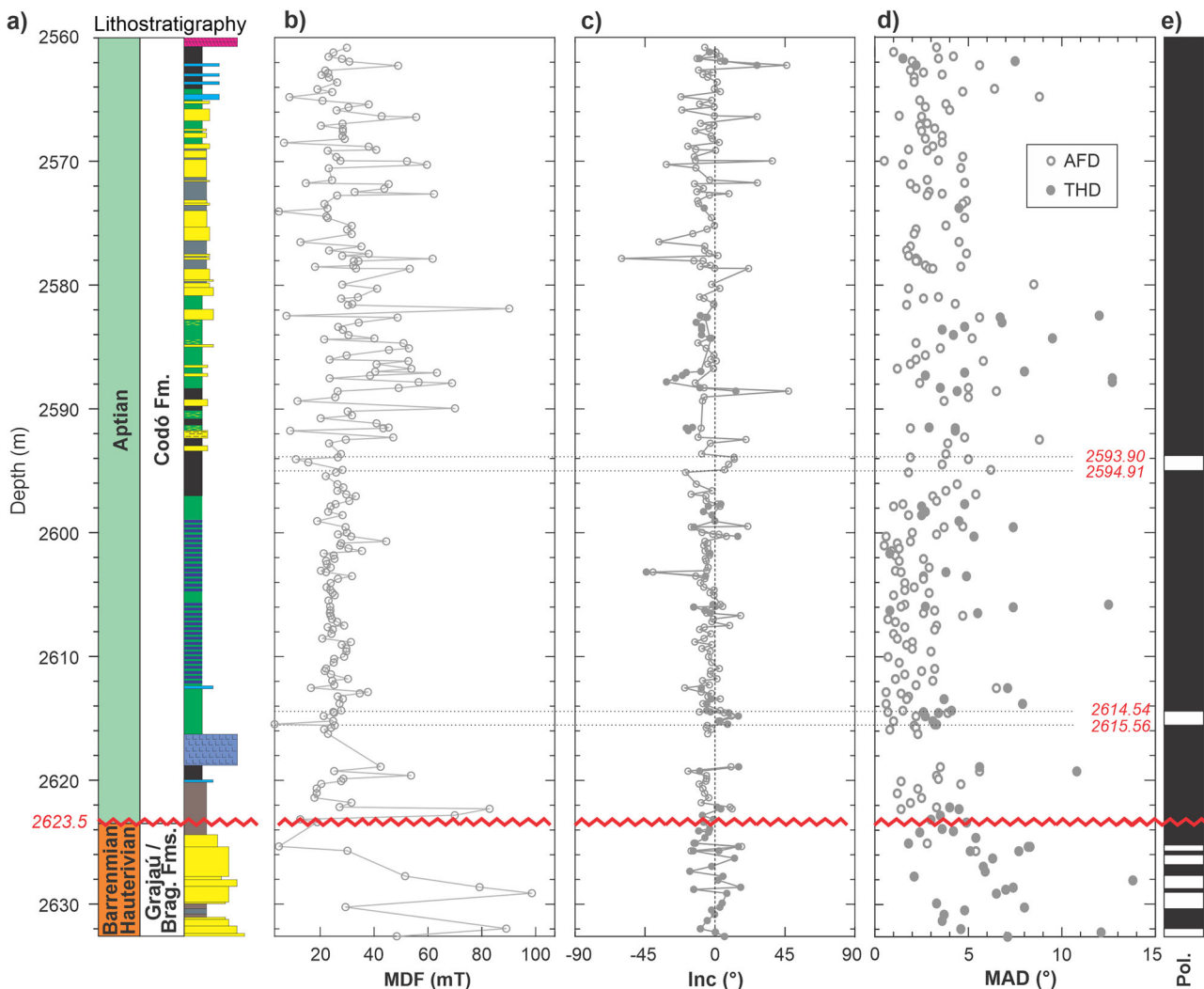


**Fig. 4 | Magnetostratigraphy analysis of the 2-ANP-5-MA core.**

**a** Lithostratigraphic scheme of the studied portion of the 2-ANP-5-MA core.

**b** Median destructive field (MDF). **c** Inclination of the magnetic field. **d** Maximum

angular deviation (MAD). **e** Geomagnetic polarity plot resulting from the ChRM directions obtained from the alternating field demagnetization (AFD) and thermal demagnetization (THD).

The South Atlantic oceanic ridge began developing around 134 Ma, with the opening progressing from south to north<sup>43</sup>. Determining the plate rotation parameters for this northward propagation requires interpolation, supported by gravimetric data<sup>1</sup>, as magnetic reversals are rare and brief during the CNPS. Plate reconstructions based on the Q1 (108 Ma) and Q2 (92 Ma) anomalies suggest the first oceanic crust in the BEM formed between 92 and 108 Ma<sup>15</sup>. Despite the 108 Ma reconstruction not showing a complete plate break-up, significant gaps, particularly in the northern part of BEM, indicate that rifting was active, allowing for marine ingress through fracture zones.

Approximately 2.7 Myr after the onset of the CNPS, a brief reversal subchron known as M-1r (or ISEA) is recorded, followed ~800 kyr later by a second short-lived reversal subchron, commonly referred to as reversal “2”<sup>18</sup>. While Chron M0r is associated with the nanofossil zone NC6<sup>44</sup> and corresponds to the lowermost Aptian<sup>22,45</sup>, the M-1r and “2” subchrons documented at DSDP Sites 463 and 402A fall within the *Globigerinelloides algerianus* planktonic foraminiferal zone and correlate with the upper Aptian *Sergipea variverrucata* Biozone (P-270)<sup>27,28</sup> (Fig. 7b, c). Cyclostratigraphic analysis constrains ISEA to  $117.03 \pm 0.14$  Ma and subchron “2” to  $116.17 \pm 0.14$  Ma, with estimated durations of ~20 kyr and ~10 kyr, respectively<sup>18</sup>. These subchrons are separated by approximately two long eccentricity (~405 kyr) cycles (Fig. 7c).

The occurrence of the P-270 Biozone (upper Aptian), together with predominantly normal polarity behavior observed in demagnetization analyses of the 2-ANP-5-MA core samples, confirms that the Codó Fm. interval in this core falls within the CNPS. Based on the duration and spacing of two short reversed intervals identified here, tuning the deeper event (2615.56–2614.54 m) gives an age of 116.94–116.91 Ma, whereas the shallower (2594.91–2593.90 m) yields 116.27–116.30 Ma—both consistent with the ages of ISEA and reversal “2” at DSDP Site 402A<sup>18</sup> (Fig. 7).

This constitutes the first evidence of short-lived polarity reversals within the CNPS documented in the BEM. The ~10 kyr difference relative to the ages reported by Ramos et al.<sup>18</sup> lies within analytical uncertainties and may reflect differences in proxy phase or sampling resolution. Additional documentation of these short-lived reversed events during the CNPS is fundamental for geodynamics, as they mark periods of slight reductions in geodynamo efficiency and variations in heat flux conditions at the core–mantle boundary, serving as key tiepoints for kinematic reconstructions.

#### Implications for refinement of kinematic models

The São Luís–Grájau Basin is part of the transtensional tectonic trough complex of the BEM<sup>3,5</sup>, and the facies and depositional system succession of well 2-ANP-5-MA core corresponds to evolutionary infill models of pull-

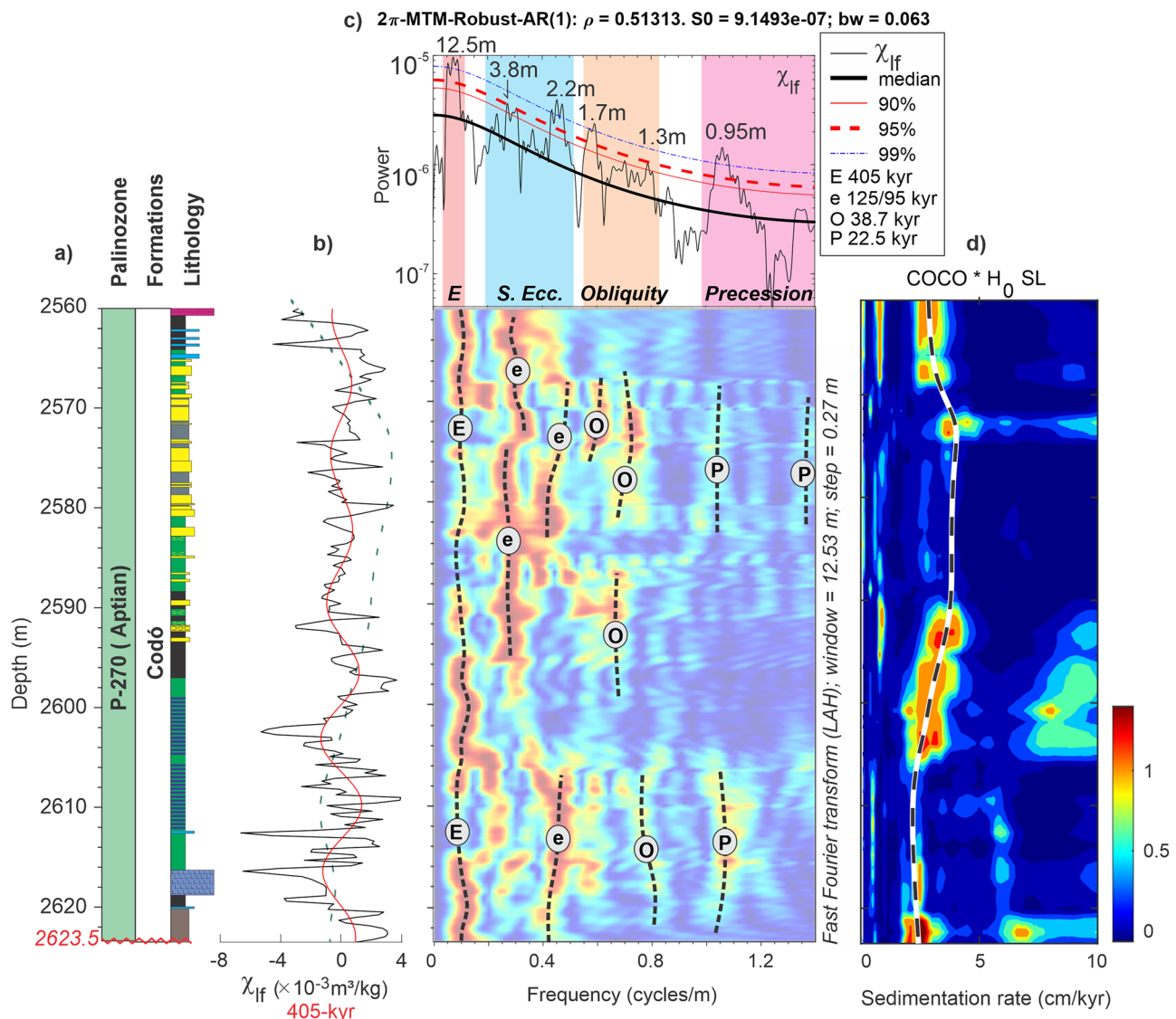


**Fig. 5 | Magneto-cyclostratigraphy analysis of the 2-ANP-5-MA core.**

**a** Lithostratigraphic column of the studied interval of the 2-ANP-5-MA core. **b** Magnetic susceptibility  $\chi_{lf}$  (black), lowess trend (green-dashed line), and 405-kyr component. **c** Multitaper spectral estimator-based spectral analysis (top) and

evolutionary spectral analysis of series (bottom), showing the interpreted cycles and the respective bands (colored rectangles). **d** COCO \*  $H_0$  SL map of 2-ANP-5-MA  $\chi_{lf}$  data, highlighting the most probable sedimentation rate track on the dashed line. E long-eccentricity, e short-eccentricity, O obliquity.

apart type basins<sup>6,23</sup>. The magneto-cyclostratigraphic analysis of the 2-ANP-5-MA core provides essential age constraints for the BEM, allowing the recorded succession of events to be placed within the Geological Time Scale (GTS) and enabling refinement of kinematic model ages. Key stages of the Gondwana breakup are captured during the transition from the continental deposits of the Grajaú/Bragança Fm. to the transitional and marine sediments of the Codó Fm. Based on our results, we refined and expanded the opening model of the BEM, reinforcing the more recent polyphased-stage opening model<sup>1,2,19,24</sup>.

The Mesozoic history of the BEM began in the Berriasian–Hauterivian, with evidence of marine presence in the region of the proto-Romanche fracture zone<sup>11</sup> (Fig. 8c). During this period, in the São Luís–Grajaú Basin, the Bragança Fm. was deposited, composed mainly of coarse clasts associated with alluvial fan systems from the rift stage, and is palynologically barren<sup>3</sup>. Overlying the Bragança Fm. are the Grajaú and Codó Fms., a sequence related to the sag phase of the São Luís–Grajaú Basin<sup>6</sup>, interpreted as a lagoonal system linked to a shallow, anoxic epicontinental sea (Codó's Sea)<sup>3–5</sup> (Fig. 8d).

Our study dated these formations through magnetostratigraphy, refining the sequence of events associated with the opening of the Equatorial Atlantic Gateway (EAG) into four deformation phases:

Stage 1 – an initial rifting stage, associated with the opening of the Central Atlantic<sup>3–5</sup>;

Stage 2 – an intraplate deformation stage (Neocomian age), related to a change in plate stress regime that accommodated northward propagation of the South Atlantic rift<sup>5</sup>;

Stage 3 – a third stage, corresponding to the thermal subsidence phase<sup>6</sup>, characterized by the establishment of a sag basin and development of the Codó epicontinental sea<sup>3,4,7,8</sup>; and

Stage 4 – a final stage, marked by the complete opening of the EAG (with deep-water circulation and mixing)<sup>10</sup>, which is beyond the scope of our study (Fig. 8).

The basal section (phase 1, ~2631–2623.5 m) of the studied interval in well 2-ANP-5-MA core is here associated with the distal facies of the Bragança Fm. Although this interval has been described as belonging to the Grajaú Fm<sup>7</sup>, the magnetic reversal pattern and magnetic mineralogy

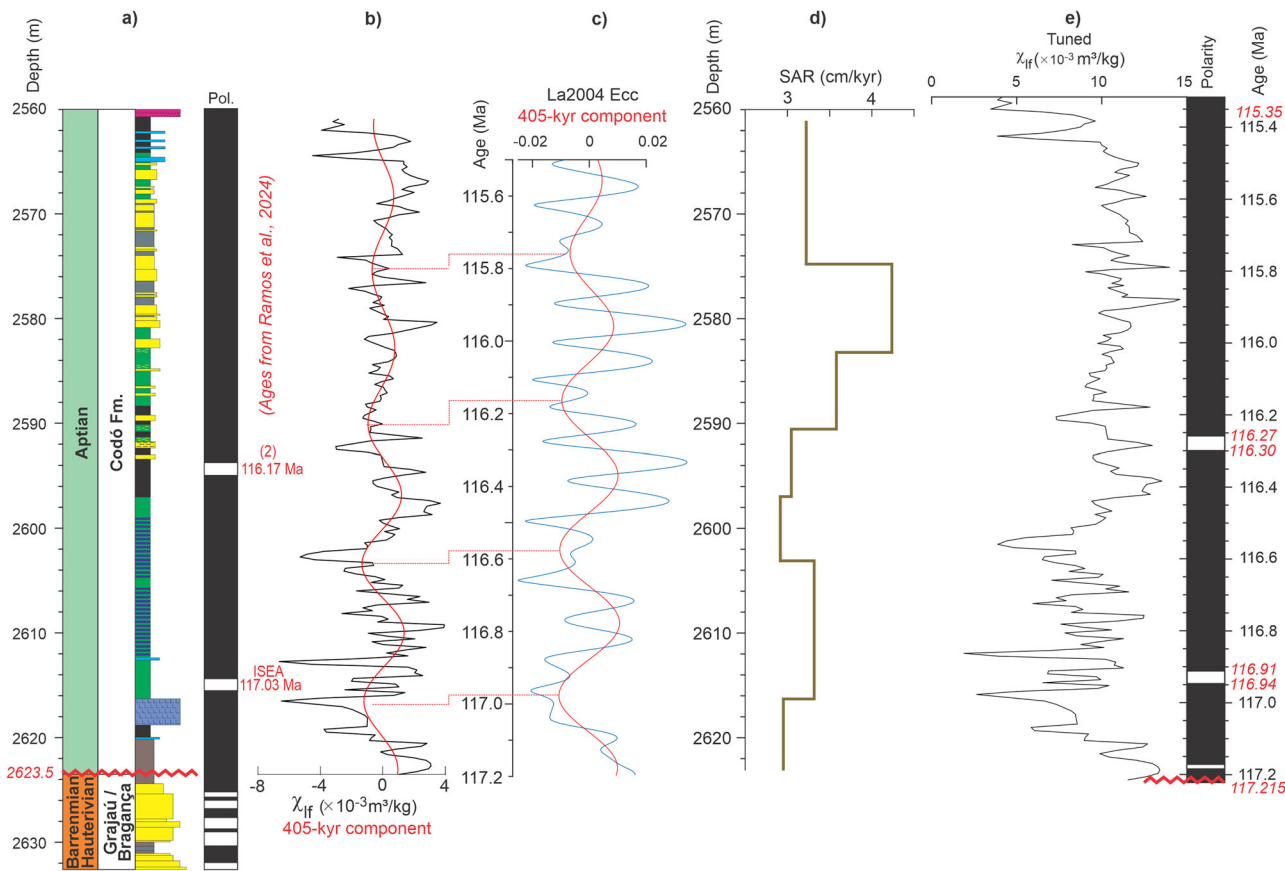


**Fig. 6 | Astronomical tuning of the 2-ANP-5-MA core.** **a** Lithostratigraphy of the 2-ANP-5-MA core and magnetic polarity obtained in this study, presenting the estimation of ages of Aptian polarity reversals during CNS (Ramos et al.<sup>18</sup>). **b** Depth-domain  $\chi_{lf}$  (black line) and 405-kyr component (red line) of 2-ANP-5-MA core.

**c** Eccentricity signal from the La2004 astronomical solution<sup>39</sup> (blue line) and its 405-kyr sinusoidal filtered component (red line). **d** Sedimentation rates (brown line) resulting from the tuning. **e** Tuned  $\chi_{lf}$  (black line) and magnetic polarity ages.

identified in our study indicate a sharp boundary between this interval and the overlying Codó Fm. Thus, the basal portion studied in well 2-ANP-5-MA was probably deposited during the rifting event related to the Central Atlantic or the Central African rifting (Fig. 8c).

In addition to the graben systems associated with Central Atlantic rifting, the central and western branches of the Central and West African Rift Systems<sup>19</sup> were also active, serving as marine water inflow pathways from the Tethys Ocean<sup>11</sup> (Fig. 8c). At this stage, besides the grabens along the São Luís–Grajaú Basin and the Calçoene Graben, other rift systems were forming, such as those of the proto-South Atlantic Ocean, the Potiguar and Recôncavo–Tucano–Jatobá grabens, and the Araripe Basin<sup>2,4,5,19</sup>.

The sedimentary response to basin evolution was a major erosional event that removed at least 10 Ma from the top of the Bragança Fm. in the São Luís–Grajaú Basin (interval between high-frequency reversals of the Hauterivian and the early Aptian, Figs. 4 and 6). This event is likely associated with the breakup of the Central Atlantic rift or even with a transgressive surface generated during the earliest marine incursions. Evidence of transpressional deformation is found along the BEM<sup>4,5</sup>. This event was dated in our study at  $117.215 \pm 0.14$  Ma, consistent with the ages proposed for stage 3 of Azevedo<sup>5</sup>, and phase 3 of Heine et al.<sup>19</sup>.

Following this unconformity, prior to the full opening of the EAG, a lower Aptian *sag* basin developed, within which the Grajaú and Codó Fms. were deposited<sup>6</sup>. These shallow-marine and evaporitic deposits represent the initial stage of the opening of the Guinea Passage<sup>2</sup>, characterized as the onset of rifting at  $\sim 117$  Ma, which led to the formation of the EAG.

Our study dated the Codó epicontinental sea<sup>3–5</sup> as a marine incursion event starting at 117.215 Ma (Fig. 8d). The tectonic configuration of a wide

*sag* basin with a dish-shaped morphology allowed marine incursions to flood large areas of central Gondwana. In addition to the marine incursions recorded in the São Luís–Grajaú Basin, several BEM basins were inundated during the Aptian transgression<sup>20</sup>.

The magneto-cyclostratigraphic study conducted in well 2-ANP-5-MA core provides absolute age control, enabling chronological refinement and improvement of tectonic reconstruction models for the early opening history of the EAG. Despite its high resolution, well-based studies are inherently local. Therefore, it is necessary to expand this type of work to other wells, increasing the geochronological dataset to compensate for the lack of radioisotopic dating and deep-tow surveys, thereby enabling the development of increasingly precise kinematic models.

#### Paleoclimatic significance of the Equatorial Atlantic connection during the Aptian

The opening of the EAG triggered substantial ocean–atmosphere reorganizations, affecting precipitation patterns and fluvial discharge along the BEM<sup>2,4,5</sup>. These environmental changes were driven by the progressive establishment of shallow epicontinental seas, disrupting the “Supercontinent Effect” that had maintained widespread arid and desert conditions across much of Gondwana<sup>7,46</sup>. During the Aptian, seawater Nd-isotope data indicate that intermediate- and deep-water mass exchange through the EAG occurred only between  $\sim 113$  and 107 Ma, remaining closed beforehand<sup>10</sup>. However, due to stratigraphic gaps and the absence of diagnostic fossils at the base of DSDP Site 364, a maximum age of  $\sim 119$  Ma can be assigned to the onset of shallow-water exchange across the EAG<sup>10</sup>.

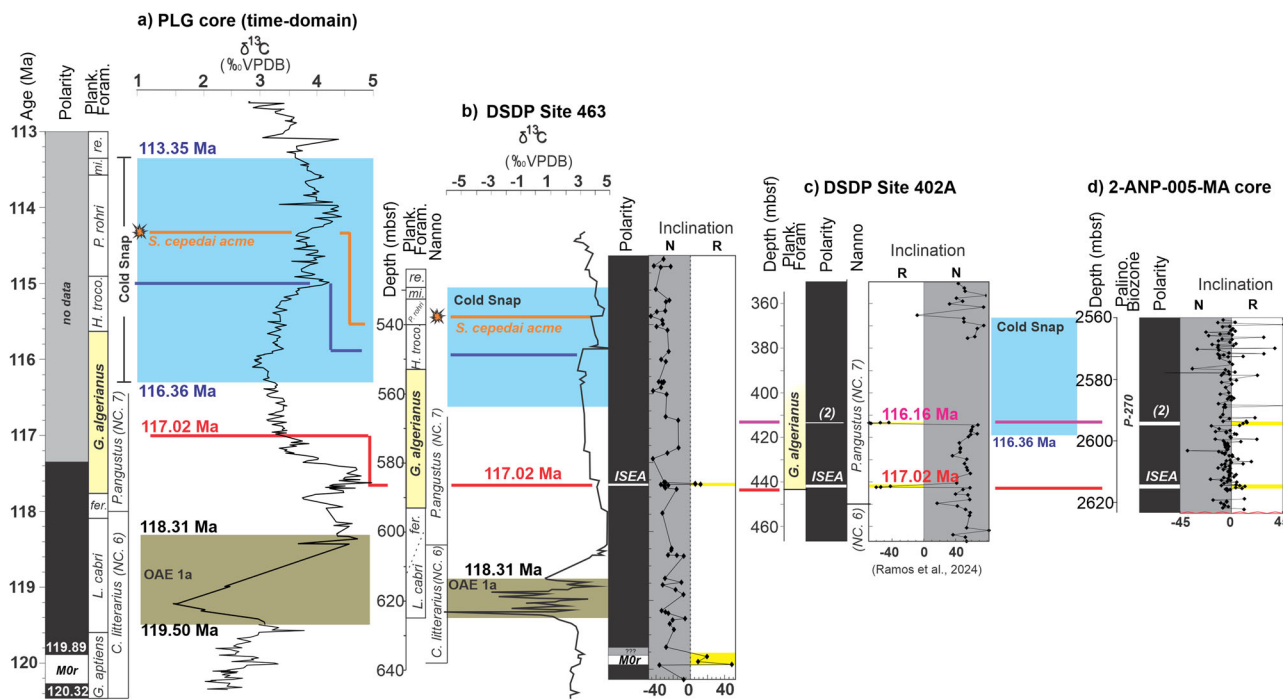


**Fig. 7 | Correlation between PLG core, DSDP sites 463 and 402A, and the 2-ANP-5-MA core.** **a** Astronomically tuned Poggio le Guaine (PLG) core events<sup>18,22,50</sup>.

*Schackoina cepedai* acme (114.4 Ma) in PLG core and DSDP Site 463. **b** DSDP Site 463, with planktonic foraminifera zone and calcareous nannofossil zones. **c** DSDP Site 402A, with planktonic foraminifera zone. M-1r and (2) reversals ages according

to Ramos et al.<sup>18</sup>. **d** 2-ANP-5-MA core (this study). P-270 biozone according to Santos et al.<sup>7</sup>. Key to planktonic and calcareous nannofossil. *mi.* = *Microhedbergella miniglobularis*, *re.* = *Microhedbergella renilaevis*, *P. rohri* = *Paratricinella rohri*, *H. troco.* = *Hedbergella trocoidea*, *G.* = *Globigerinelloides*, *fer.* = *ferreolensis*, *L.* = *Leupoldina*, *C.* = *Chiastozygus*, *S.* = *Shackoina*.

Carbon isotope and biomarker correlations show that by ~118 Ma, South Atlantic waters — via the Walvis–Rio Grande gateway — had already reached the Sergipe Basin (Fig. 8c–e)<sup>26,47</sup>, indicating a connection between the southern and central Atlantic during the early Aptian. At the same time, Aptian marine transgressions entered lacustrine systems of BEM basins<sup>2,4,20</sup>, transforming continental environments into marine ones and promoting evaporite deposition. In 2-ANP-5-MA core, this event is recorded by halite and anhydrite beds dated at 117.215 Ma, marking the earliest marine incursions in the São Luís–Grajaú Basin. The extent of these floods increased gradually over the next ~0.86 Myr, culminating in the establishment of the EHB at 116.36 Ma. This milestone coincides with a major marine flooding event, evidenced by the occurrence of the dinocyst *Subtilisphaera*<sup>20,27,46</sup> (Fig. 8a). During this interval, the “carbonate factory” (carbonate–shale sequence, 2620–2597 m) was replaced by deltaic deposits with a basal black shale, associated with the *G. algerianus* planktonic foraminiferal zone (Fig. 8a, b). Increases in the Wet/Dry ratio in other BEM basins indicate that this environmental shift — from arid to humid conditions in Gondwana<sup>7,8,46</sup> — had a regional scope. The ~1 Myr lag between marine incursions in the Sergipe Basin and in the BEM suggests that, although evidence exists for northward marine entry<sup>20</sup>, a southward pathway cannot be ruled out. Transitional conditions persisted throughout the Aptian, until fully marine environments became established in the Albian<sup>2,4,5,19</sup>.

The chronology obtained here indicates that the onset of the gradual opening of the EAG coincided with progressive changes in sea-surface temperature<sup>18,49</sup> and with the development of major Cretaceous Oceanic Red Beds in the Tethys<sup>20,50</sup>. This suggests that the formation of extensive epicontinental seas during the *sag* phase of the São Luís–Grajaú Basin (Fig. 8d) influenced the global climate system by enhancing ocean ventilation, displacing the proto–ITCZ, and fostering the establishment of the EHB. The magneto–cyclostratigraphic age of the first marine incursions aligns with a pronounced cooling event recorded by TEX<sub>86</sub> thermometry<sup>48</sup>, amplifying the cooling trend that culminated in the Aptian Cold Snap<sup>13,49</sup>. Combined with enhanced carbon burial during the latest Aptian–earliest

Albian<sup>5,13,47</sup>, these processes likely drove cooling within the mid-Cretaceous greenhouse context. This climatic reorganization, linked to the peak of the global Cold Snap, allows long-distance correlations among BEM basins (Fig. 8a, b) and reinforces the hypothesis of Santos et al. (2022)<sup>7</sup> connecting proto–ITCZ displacement to the Cold Snap.

A ~2 Myr cycle of alternating arid and humid phases, as evidenced by evaporite deposition at both ends of the studied interval (Fig. 8a), was likely paced by the long-eccentricity astronomical grand cycles. These grand cycles, together with sustained changes in ocean circulation, influenced sedimentation and organic carbon burial, modulated by variations in fluvial discharge, sea level, and lacustrine extent<sup>41,51,52</sup>.

The breakup of Gondwana was among the most significant geological events of the Cretaceous. The associated climatic changes unfolded relatively gradually, marked by a progressive Aptian cooling linked to the protracted opening of the South Atlantic Ocean. After the complete separation of the South American and African plates at ~113 Ma — with the onset of deep-water mass exchange — high temperatures typical of the Cretaceous greenhouse likely re-emerged, possibly due to reduced carbon burial (Fig. 8d). The results of this study provide a robust chronostratigraphic calibration of Aptian events related to the opening of the South Atlantic along the Equatorial Margin. They improve constraints on the timing and causes of paleoenvironmental change, supporting future global paleoclimate assessments through magnetostratigraphic and isotopic correlations. The identification of short-lived geomagnetic reversals in the equatorial region offers key temporal anchors within the Cretaceous Normal Polarity Superchron, enabling refined models for the opening of the Atlantic Ocean and guiding further investigations in other sedimentary records.

## Methods

### Geological setting

The BEM is characterized by three east-west oriented oceanic fracture zones—St. Paul, Romanche, and Chain FZs—that separate margin segments, influenced by dextral strike-slip plate motion and forming a series

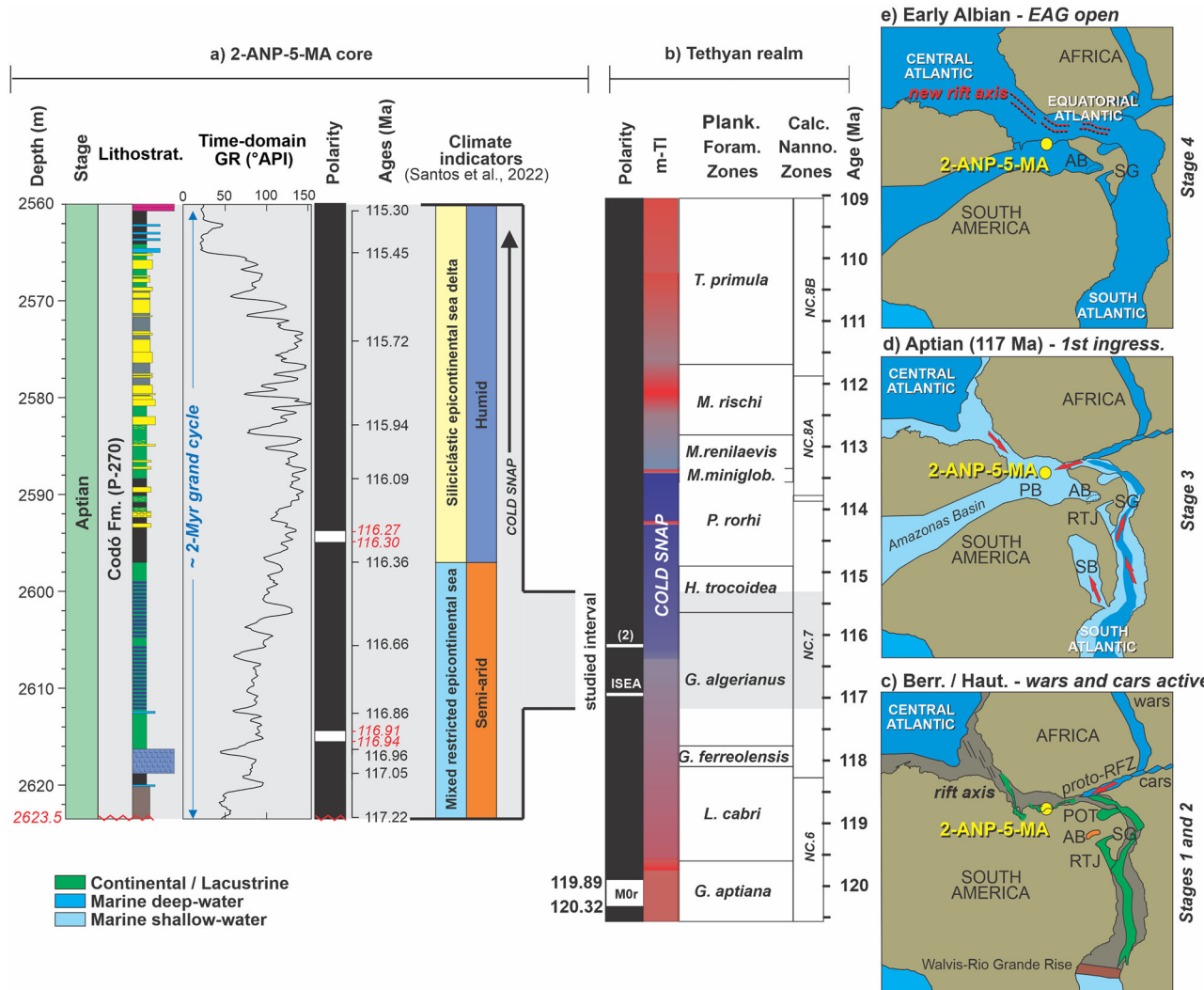


**Fig. 8 | Time-domain correlation between the 2-ANP-5-MA core and PLG core (Tethyan realm). a** Right: Lithostratigraphy of the 2-ANP-5-MA core, Time-domain GR profile and magnetic polarity obtained in this study. Left: Climate indicators<sup>7</sup> expressing the change of the semi-arid conditions to humid conditions. The estimative of the onset of the cold snap ages from Leandro et al.<sup>22</sup>. **b** Simplified timescale showing magnetic polarity ages (this study and Ramos et al.<sup>18</sup>), planktonic foraminiferal, calcareous nannofossils zones and OAE 1a age<sup>22</sup>. M0r Chron is correlated with *G. aptiensis* planktonic foraminifera and *C. litterarius* calcareous nannofossil zones, and ISEA and “2” Subchrons are associated with *G. algerianus* planktonic foraminifera and NC6 (*R. angustus*) calcareous nannofossil zones. **c** Stages 1 and 2 – Schematic reconstruction of the Berriasian–Hauterivian interval,

showing the location of the proto–Romanche Fracture Zone (RFZ), connecting the WARS (West African Rift System) and the CARS (Central African Rift System) to the future BEM. **d** Stage 3 – Schematic reconstruction of the Aptian interval (~117 Ma), showing the area of the BEM where the Codó Sea<sup>3,4</sup> was established, with possible directions of marine entry (red arrows). **e** Stage 4 – Schematic reconstruction of the Albian interval, representing the time when the complete separation of the South American and African plates occurred. Schematic reconstructions based on kinematic models<sup>1,2,5,19</sup>. RFZ Romanche Fracture Zone, POT Potiguar Basin, SG Sergipe Basin, RTJ Recôncavo–Tucano–Jatobá Basins, AB Araripe Basin, PB Parnaíba Basin, SB São Francisco Basin.

of oblique steps<sup>1,6,19</sup>. This region is classified as an oblique margin, where transform faults segment pull-apart sedimentary basins due to seafloor spreading propagating northward toward the Equatorial Atlantic Ocean. The São Luís–Grajaú sedimentary basin, located in the north-northeastern region of Brazil, is one of the basins that experienced predominantly transtensive tectonics during the Aptian and Albian stages<sup>3–5</sup>. It is separated from the northern maritime basins by the Ilha de Santana Platform, while to the south, it is in contact with the Ferrer–Urbano Santos Arc<sup>6</sup>. Together, these geological characteristics highlight the complex tectonic evolution of the region, with the São Luís basin playing a significant role in the broader dynamics of the BEM during the Mesozoic. The 2-ANP-5-MA drill site (lat. 2°14' 45.32" N; long. 45°54' 54.32" E) is located on the São Luís sedimentary basin (Fig. 1c). The sediments collected in this core comprises the Aptian–Albian interval of the São Luís–Grajaú Basin<sup>7,8</sup>. The core either seated directly on the

basement of the São Luís Craton or overlying Paleozoic sediments<sup>6–8</sup>. This core sampled 2914 m of various lithologies (Fig. 1e). From the top to 2469 m, collected sandstones of the Itapecuru Fm., passing through the entire Codó Fm. until reaching a disconformity that separates it from the Grajaú/Bragança Fm. at 2630 m (Fig. 1e). Before encountering the crystalline basement, it traversed ~50 m of a Paleozoic sequence (composite profile, <https://reate.cprm.gov.br/arquivos/index.php/s/j2vquXFrz05VzUg?path=%2FPOCO%2FCategoria-2%2F2-ANP-5-MA%2FPerfil%20Compuesto>). The Codó Fm. (Aptian–Albian) records thick layers of shale, in addition to other evaporitic, carbonate, and siliciclastic facies. Fishes, mollusks, dinoflagellates cysts, and foraminifers indicate the presence of marine conditions in the Codó Fm. in the São Luís Basin, associated with the biozone P-270 (*Sergipea variverrucata*) which corresponds to the Late Aptian<sup>27,28</sup>. The 2-ANP-5-MA core, although it passed through the entire Codó Fm. (2470–2623.5 m), fully recorded the

lower section of the Codó Fm. (from 2560 m). Biozone (P-270) was identified in the same well by Santos et al. (2022)<sup>7</sup>.

### Rock magnetism and sampling strategy

Paleomagnetic and rock magnetic measurements were performed at the Laboratory of Paleomagnetism and Geomagnetism of the University of São Paulo (USPMag) and at the Laboratory of Paleomagnetism and Magnetic Mineralogy of the Brazilian National Observatory (LPC2M-ON). A total of 454 discrete cubic samples within ~8 cm<sup>3</sup> of 2-ANP-5-MA were selected and submitted to magnetic measurements to obtain paleodirection of the characteristic remanent magnetization. To assess the magnetic carrier of the representative sediments samples were selected for rock magnetism measurements. Magnetic susceptibility was measured using an MFK2-FA Multi-Function Kappabridge in a frequency of 976 Hz in a field of 200 A/m. Remanence measurements were obtained using a three-axis 2G Enterprises model 755 SQUID Long-Core magnetometer in a magnetically shielded room housed in USPMag. A pilot analysis was initially performed with a larger number of steps. The samples were submitted to stepwise alternating field demagnetization (AFD) over 17 steps of 0, 2, 4, 7, 10, 15, 20, 25, 30, 35, 40, 50, 60, 70, 80, 90, 100 mT. Thermal demagnetization (THD) were measured in the sister samples by stepwise heating at 0, 50, 100, 150, 200, 250, 300, 350, 400, 450, 500, 550, 560, 580, 600, 620, 640, 660, 680 °C. The characteristic remanent magnetization, i.e., paleomagnetic inclination, declination, and the maximum angle of deviation (MAD) were calculated using the vector end-point demagnetization diagrams<sup>53</sup> and Principal Component Analysis (PCA). The calculation of the paleomagnetic directions was performed by fitting a linear regression that minimized the maximum angular deviation (max. 10° for alternating-field and 15° for thermal demagnetization). Anchoring to the origin was not necessary for most samples; however, it was applied to a few samples to improve the MAD. Since the core was not azimuthally oriented, no reliable paleomagnetic declination of the samples could be obtained. The MDF is measurement of the 'strength' required to demagnetize half of a sample's natural remanent magnetization, serving as a proxy for the average coercivity of the magnetic minerals present. The MDF is a parameter used to characterize the magnetic stability of a sample when subjected to alternating field (AF) demagnetization (the value of the alternating field that removes 50% of the sample's natural remanent magnetization). After the measurement of NRM, an anhysteretic remanent magnetization (ARM) was acquired in 17 steps of 0, 2, 4, 7, 10, 15, 20, 25, 30, 35, 40, 50, 60, 70, 80, 90, and 100 mT alternating field (AF) in the presence of an axial 0.05 mT bias field and then AF demagnetized in the same steps. The ARM at 100 mT represents the concentration of fine-grained magnetite and is sensitive to low coercivity minerals<sup>30</sup>. The isothermal remanent magnetization (IRM) was acquired using a 2G pulse magnetic field inductor, and the remanence was measured. For all samples a pulse-field of 1 T was applied, to obtain the saturation IRM (SIRM). The SIRM detects the relative amounts of a low coercivity ferromagnetic minerals, such as magnetite, compared to the amounts of a high coercivity antiferromagnetic minerals, such as hematite<sup>30,31</sup>. Then a back-field of 100 mT and 300 mT were applied to obtain the IRM<sub>100mT</sub> and IRM<sub>300mT</sub>, respectively. From these measurements the S-ratio (S-ratio = IRM<sub>300mT</sub>/SIRM), L-ratio ((SIRM + IRM<sub>300mT</sub>) / (SIRM + IRM<sub>100mT</sub>)) and the "hard" IRM (HIRM = (SIRM + IRM<sub>300mT</sub>)/2) were calculated<sup>52</sup>. In addition, and as a first estimate of relative magnetic grain-size variation, the median destructive field of the NRM (MDF) was determined. The S-ratio is a measure of the relative abundance of high-coercivity minerals mixed with ferrimagnetic minerals<sup>52</sup>. When the S-ratio approaches unity, it suggests that low-coercivity minerals, such as magnetite and maghemite, are the dominant magnetic minerals in the samples. In contrast, when the S-ratio is close to zero, the contributions of hematite and/or goethite become significant<sup>52</sup>. The L-ratio is used to quantify the relative concentrations of hematite and/or goethite in mineral mixtures, suggesting variations in sediment provenance<sup>31,52</sup>. The HIRM is a measure of the mass concentration of high-coercivity magnetic minerals. Furthermore, we combined magnetic

parameters to form SIRM/χ<sub>lf</sub> and ARM<sub>100mT</sub>/SIRM. The ARM<sub>100mT</sub>/SIRM is an indicator of the amount of large fraction of SD-PSD particles, and it is indicative that magnetite grain size<sup>30,31</sup>. Hysteresis loops and IRM acquisition curves were measured for seven representative samples along the cores (2560–2630 m). The samples were analyzed in a Vibrating Sample Magnetometer (VSM) MicroMagTM3900 at USPMag. Approximately 1 g of sediment from each sample was prepared and measured for hysteresis loops and IRM acquisition, and backfield curves up to 1 T at room temperature. The hysteresis data were subsequently processed using HystLab<sup>54</sup> to correct instrumental drift and extract magnetic parameters. These results allow one to identify the domain state(s) and magnetic interactions among magnetic particles<sup>36</sup>. The determination of different magnetic phases and domains was performed through the interpretation of FORC (First Order Reversal Curve) diagrams<sup>55</sup> of the representative samples. The measurements to obtain the FORC distributions were conducted at room temperature for four samples, applying fields up to 1 T using the same VSM. FORC diagrams were processed using FORCinel<sup>56</sup>, with adaptive smoothing parameters Sc0 = 4, Sc1 = 7, Sb0 = 4, and Sb1 = 7. These values control smoothing along the coercivity and interaction field axes, reducing noise and improving the resolution of magnetic domain distributions. Thermomagnetic analyses were performed in 18 representative powdered samples using a CS-4 furnace attached to the MFK2-FA Kappabridge housed at the LPC2M-ON. The magnetic susceptibility was measured while heating the sample up to 700 °C and cooling it down to room temperature. The measurements were carried out in an argon atmosphere to avoid material oxidation. Given the predominantly continental sedimentary context of the EAG opening and the scarcity of magnetic and radioisotopic data, magnetostratigraphy is essential for establishing an accurate age model, anchored in the GTS<sup>42</sup>. Magnetostratigraphy offers significant benefits for global correlation, as the reversal process is geologically synchronous and nearly instantaneous worldwide. When combined with astrochronology and a biostratigraphic framework (even at low resolution), magnetostratigraphy becomes known as magneto-cyclostratigraphy. This technique allows sediments to be dated with unprecedented accuracy, precision, and resolution that cannot be achieved by any other dating method.

### Cyclostratigraphy

Cyclostratigraphic analyses for low-field magnetic susceptibility dataset (χ<sub>lf</sub>) were conducted with Acycle version 2.4.1<sup>57</sup> and Astrochron Version 1.2<sup>58</sup>. Since the studied interval exhibits complex lithological variation, we chose to use χ<sub>lf</sub> instead of gamma-ray, as the χ<sub>lf</sub> signal is more independent of lithology, making it more reliable. After interpolation (every 27 cm) the datasets were detrended using a Lowess method (window = 25 m). Spectral analysis was conducted using the prolate multitaper spectral estimator, comparing it against a robust red noise null model, with confidence levels set at the mean, 90%, 95% and 99%. The 405-kyr long eccentricity sinusoidal curve was carried out from a gaussian bandpass filtering (0.05–1.20 cycles/m) applied to the χ<sub>lf</sub> dataset to isolate the interpreted long eccentricity component sinusoidal curve from the datasets tuned according to the g<sub>2</sub>-g<sub>5</sub> target curve from La2004 astronomical solution<sup>41</sup>, prior to the tuning process. Additionally, we performed evolutionary Fast Fourier Transform analyses to observe continuity of the spectral frequencies along χ<sub>lf</sub> series. The sediment accumulation rates were evaluated throughout the 2-ANP-5-MA studied interval using COCO/eCOCO<sup>59</sup> and ASM<sup>38</sup>. We conducted the COCO/eCOCO analysis using 2000 Monte Carlo simulations, applying sedimentation rates ranging from 0.26 to 10 cm/kyr, referenced to the La2004 solution with a median age of 116 Ma (maximum frequency of 0.06/kyr), employing the Pearson correlation method.

### Data availability

The χ<sub>lf</sub> and paleomagnetic direction datasets used in this study are available in the supplementary materials (Supplementary Data 1 and 2) and zenodo repository at <https://zenodo.org/records/17298755>.

## Code availability

All analyses were performed with the freeware HystLab<sup>54</sup>, Acycle version 2.4.1<sup>57</sup>, Astrochron R Package Version 1.2<sup>58</sup> and Gplates<sup>60</sup>.

Received: 23 May 2025; Accepted: 13 October 2025;

Published online: 24 November 2025

## References

- Pérez-Díaz, L. & Eagles, G. South Atlantic paleobathymetry since early Cretaceous. *Sci. Rep.* **7**, 11819 (2017).
- Duarte, D. et al. Early Cretaceous deep-water bedforms west of the Guinea Plateau revise the opening history of the Equatorial Atlantic Gateway. *Glob. Planet. Change* **249**, 104777 (2025).
- Lima, M. R., Aranha, L. G. & Feijó, F. J. Bacias de Bragança-Viseu, São Luís e Gráben de Ilha Nova. *Bol. de Geociências da Petrobras* **8**, 111–116 (1994).
- Soares Júnior, A. V., Hasui, Y., Costa, J. B. S. & Machado, F. B. Evolução do rifteamento e paleogeografia da margem Atlântica Equatorial do Brasil: Triássico ao Holoceno. *Geociências* **669** <https://www.periodicos.rc.biblioteca.unesp.br/index.php/geociencias/article/view/5593> (2011).
- Azevedo, R. P. *Tectonic Evolution of Brazilian Equatorial Continental Margin Basins* (Imperial College) <https://doi.org/10.1306/D9CB69C5-1715-11D7-8645000102C1865D> (1991).
- Zalán, P. V. Bacias de Bragança-Viseu, São Luís e Ilha Nova. *B. Geoci. Petrobras* **15**, 341–345 (2007).
- Santos, A. et al. Earlier onset of the Early Cretaceous Equatorial humidity belt. *Glob. Planet. Change* **208**, 1–14 (2022).
- Gonzalez, L. D. C., Mastalerz, M. & Mendonça-Filho, J. G. Application of organic facies and biomarkers in characterization of paleoenvironmental conditions and maturity of sediments from the Codó Formation in the west-central part of the São Luís Basin. *Brazil Int. J. Coal Geol.* **225**, 103482 (2020).
- Haq, B. U. Cretaceous eustasy revisited. *Glob. Planet. Chang.* **113**, 44–58 (2014).
- Dummann, W. et al. The early opening of the Equatorial Atlantic gateway and the evolution of Cretaceous peak warming. *Geology* **51**, 476–480 (2023).
- Bonatti, E. et al. Lower Cretaceous deposits trapped near the equatorial Mid-Atlantic Ridge. *Nature* **380**, 518–520 (1996).
- Jenkyns, H. Geochemistry of oceanic anoxic events. *Geochem. Geophys. Geosyst.* **11**, <https://doi.org/10.1029/2009GC002788> (2010).
- McAnena, A. et al. Atlantic cooling associated with a marine biotic crisis during the mid-cretaceous period. *Nat. Geosci.* **6**, 558–561 (2013).
- Kent, D. V. & Gradstein, F. M. A Cretaceous and Jurassic geochronology. *Geol. Soc. Am. Bull.* **96**, 1419–1427 (1985).
- Granot, R., Dymant, J. & Gallet, Y. Geomagnetic field variability during the Cretaceous normal superchron. *Nat. Geosci.* **5**, 220–223 (2012).
- VandenBerg, J., Klootwijk, C. T. & Wonders, A. A. H. The Late Mesozoic and Cenozoic movements of the Umbrian Peninsula: Further paleomagnetic data from the Umbrian sequence. *Geol. Soc. Am. Bull.* **89**, 133–155 (1978).
- Zhang, D. et al. Frequent polarity reversals in the cretaceous normal superchron. *Geophys. Res. Lett.* **48**, <https://doi.org/10.1029/2020GL091501> (2021).
- Ramos, J. M. F. et al. Orbital tuning of short reversed geomagnetic polarity intervals in the Cretaceous Normal Polarity Superchron. *Geophys. Res. Lett.* **51**, e2024GL110530 (2024).
- Heine, C., Zoethout, J. & Müller, R. D. Kinematics of the South Atlantic rift. *Solid Earth* **4**, 215–253 (2013).
- Arai, M. Paleogeografia do Atlântico Sul no Aptiano: um novo modelo a partir de dados micropaleontológicos recentes. *Bol. Geocienc. da Petrobras* **17**, 331–351 (2009).
- Fauth, G. et al. Early Aptian marine incursions in the interior of northeastern Brazil following the Gondwana breakup. *Sci. Rep.* **13**, 6728 (2023).
- Leandro, C. G. et al. Astronomical tuning of the Aptian stage and its implications for age recalibrations and paleoclimatic events. *Nat. Commun.* **13**, 2941 (2022).
- Umhoefer, P. J. et al. Breaching of strike-slip faults and successive flooding of pull-apart basins to form the Gulf of California seaway from ca. 8–6 Ma. *Geology* **46**, 695–698 (2018).
- Basile, C. et al. The Jurassic magmatism of the Demerara Plateau (offshore French Guiana) as a remnant of the Sierra Leone hotspot during the Atlantic rifting. *Sci. Rep.* **10**, 7486 (2020).
- Lúcio, T., Neto, J. A. S. & Selby, D. Late Barremian/early Aptian Re-Os age of the Ipubi Formation black shales: stratigraphic and paleoenvironmental implications for Araripe Basin, northeastern Brazil. *J. South Am. Earth Sci.* **102**, 1–13 (2020).
- Cui, X., Wignall, B., Freeman, K. H. & Summons, R. E. Early Cretaceous marine incursions into South Atlantic rift basins originated from the South. *Nat. Commun. Earth Environ.* **4**, 6 (2023).
- Regali, M. S. & Santos, P. R. S. Palinoestratigrafia e geocronologia dos sedimentos albo-aptianos das bacias de Sergipe e de Alagoas – Brasil. In *Boletim do 5º Simpósio sobre o Cretáceo do Brasil*, (eds, Dias-Brito, D., de Castro, J. C. & Rohn, R.) 411–419 (Serra Negra, 1999).
- Koutsoukos, E. A. *Mid- to Late Cretaceous Microbiostratigraphy Paleoecology and Paleobiography of the Sergipe Basin*. Plymouth University, UK, <https://doi.org/10.24382/3868> (1989).
- Tauxe, L. Sedimentary records of relative paleointensity of the geomagnetic field: theory and practice. *Rev. Geophys.* **31**, 319–354 (1993).
- Kodama, K. P. *Paleomagnetism of Sedimentary Rocks*. First Edit. John Wiley & Sons, Ltd: Chichester, UK, 2012.
- Liu, Q. et al. Environmental magnetism: principles and applications. *Rev. Geophys.* **50**, <https://doi.org/10.1029/2012RG000393> (2012).
- Roberts, A. P., Cui, Y. & Verosub, K. L. Wasp-waisted hysteresis loops: mineral magnetic characteristics and discrimination of components in mixed magnetic systems. *J. Geophys. Res. Solid Earth* **100**, 17909–17924 (1995).
- Tauxe, L., Mullender, T. A. T. & Pick, T. Potbellies, wasp-waists, and superparamagnetism in magnetic hysteresis. *Solid Earth* **101**, 571–583 (1996).
- Roberts, A. P. et al. Unlocking information about fine magnetic particle assemblages from first-order reversal curve diagrams: recent advances. *Earth Sci. Rev.* **227**, 103950 (2022).
- Carvalho, C., Muxworthy, A. R. & Dunlop, D. First order reversal curve (FORC) diagrams of magnetic mixtures: Micromagnetic models and measurements. *Phys. Earth Planet. Inter.* **154**, 308–322 (2006).
- Day, R., Fuller, M. & Schmidt, V. A. Hysteresis properties of titanomagnetites: grain-size and compositional dependence. *Phys. Earth Planet. Inter.* **13**, 260–267 (1977).
- Tauxe, L. Lectures in Paleomagnetism, by Lisa Tauxe. Available at: <http://earthref.org/MAGIC/books/Tauxe/2005/> (2005).
- Roberts, A. P., Tauxe, L., Heslop, D., Zhao, X. & Jiang, Z. A critical appraisal of the “Day” diagram. *J. Geophys. Res. Solid Earth* **123**, 2618–2644 (2018).
- Dunlop, D. J. & Özdemir, Ö. *Rock Magnetism Fundamentals and Frontiers*. Cambridge University Press, Cambridge. <https://doi.org/10.1017/CBO9780511612794> (1997).
- Waltham, D. Milankovitch period uncertainties and their impact on cyclostratigraphy. *J. Sediment. Res.* **85**, 990–998 (2015).
- Laskar, J. et al. A long-term numerical solution for the insolation quantities of the Earth. *Astron. Astrophys.* **428**, 261–285 (2004).
- Gale, A. S. et al. The Cretaceous period. In *Geologic Time scale 2020*, 1023–1086 (Elsevier, 2020).
- Channell, J. E. T., Erba, E., Nakanishi, M. & Tamaki, K. Late Jurassic-Early Cretaceous time scales and oceanic magnetic anomaly block models. In: *Geochronology, Time Scales and Global Stratigraphic*

*Correlation*, (ed. Berggren, William A.) *SEPM Special Publications* 54, 51–63. SEPM, <https://doi.org/10.2110/pec.95.04.0051> (1995).

44. Bralower, T. J. et al. Timing and paleoceanography of oceanic Dysoxia/Anoxia in the late Barremian to Early Aptian (Early Cretaceous). *Palaios* **9**, 335–369 (1994).
45. Savian, J. et al. The Barremian-Aptian boundary in the Poggio le Guaine core (central Italy): evidence for magnetic polarity Chron M0r and oceanic anoxic event 1a. *Geol. Soc. Am. Spec. Pap.* **524**, 57–78 (2016).
46. Carvalho, M. A. et al. Late Aptian (Early Cretaceous) dry-wet cycles and their effects on vegetation in the South Atlantic: Palynological evidence. *Cretaceous Res.* **100**, 172–183 (2019).
47. Tedeschi, L. et al. Aptian carbon-isotope record from the Sergipe-Alagoas Basin: new insights into oceanic anoxic event 1a and the timing of seawater entry into the South Atlantic. *Newsl. Stratigr.* **53**, <https://doi.org/10.1127/nos/2019/0529> (2019).
48. O'Brien, C. L. et al. Cretaceous sea-surface temperature evolution: constraints from TEX86 and planktonic foraminiferal oxygen isotopes. *Earth Sci. Rev.* **172**, 224–247 (2017).
49. Bottini, C. & Erba, E. Mid-Cretaceous paleoenvironmental changes in the western Tethys. *Clim. Past* **14**, 1147–1163 (2018).
50. Coccioni, R. et al. Umbria-Marche Basin, Central Italy: a reference section for the Aptian-Albian interval at low latitudes. *Sci. Drilling* **13**, <https://doi.org/10.2204/iodp.sd.13.07.2011> (2012).
51. Liu, Y. et al. Oscillations of global sea-level elevation during the Paleogene correspond to 1.2-Myr amplitude modulation of orbital obliquity cycles. *Earth Planet. Sci. Lett.* **522**, 65–78 (2019).
52. Liu, Q., Roberts, A. P., Torrent, J., Horng, C. & Larrasoña, J. C. What do the HIRM and S-ratio really measure in environmental magnetism?. *Geochem. Geophys. Geosyst.* **8**, Q01Z10 (2007).
53. Zijderveld, J. D. A. A. C. Demagnetization of rocks: analysis of results. In *Methods in Palaeomagnetism* 254–286 (Elsevier, 1967).
54. Paterson, G. A., Zhao, X., Jackson, M. & Heslop, D. Measuring, processing, and analyzing hysteresis data. *Geochem. Geophys. Geosyst.* **19**, 1925–1945 (2018).
55. Roberts, A. P., Pike, C. R. & Verosub, K. L. First-order reversal curve diagrams: a new tool for characterizing the magnetic properties of natural samples. *J. Geophys. Res. Solid Earth* **105**, 28461–28475 (2000).
56. Harrison, R. J. & Feinberg, J. M. FORCinel: an improved algorithm for calculating first-order reversal curve distributions using locally weighted regression smoothing. *Geochem. Geophys. Geosyst.* **9**, Q05016 (2008).
57. Li, M., Hinnov, L. & Kump, L. Acycle: time-series analysis software for paleoclimate research and education. *Comput. Geosci.* **127**, 12–22 (2019).
58. Meyers, S. R. Astrochron. *An R Package for Astrochronology* <https://cran.r-project.org/package=astrochron> (2014).
59. Li, M. S., Kump, L. R., Hinnov, L. A. & Mann, M. E. Tracking variable sedimentation rates and astronomical forcing in Phanerozoic paleoclimate proxy series with evolutionary correlation coefficients and hypothesis testing. *Earth Planet. Sci. Lett.* **501**, 165–179 (2018).
60. Müller, R. D. et al. GPlates: building a virtual Earth through deep time. *Geochem. Geophys. Geosyst.* **20**, 2669–2691 (2019).

## Acknowledgements

This study was financially supported by the Specialization and Postgraduate Program of Petrobras. J.M.F. RAMOS thanks Petrobras for Ph.D. process. The paper is a part of the projects *Processamento e interpretação de dados magnetoestratigráficos do Cretáceo das Bacias Brasileiras* and *Magneto-cicloestratigrafia do Cretáceo na Margem Equatorial Brasileira (MEQ)*, both financed by Petróleo Brasileiro S.A.—Petrobras (FAURGS 8368 and 8892). J.F.S. also thanks CNPq for grants #304022/2018-7 and #311231/2021-7. D.R.F. thanks the Foundation Carlos Chagas Filho Research Support of the

State of Rio de Janeiro (FAPERJ—grant #E-26/200.931/2022) and CNPq (grant #314462/2020-1). We thank the ANP (Agência Nacional de Petróleo) for granting permission to collect and analyze the palaeomagnetic samples from well 2-ANP-005-MA, drilled by PETROBRAS. The authors sincerely thank Editorial Board Member Deborah Tangunan and Associate Editor Dr. Alireza Bahadori for their suggestions and reviews. We would also like to thank reviewers Tim van Peer, Dan V. Palcu Rolier and Debora P. Duarte for their valuable suggestions and comments during the peer-review process.

## Author contributions

J.M.F.R.: conceptualization, methodology, validation, cyclostratigraphic and paleomagnetic analyses, astronomical tuning, project administration, and writing. J.F.S.: conceptualization, methodology, validation, paleomagnetic analysis, investigation, writing, project administration, and funding acquisition. D.R.F.: methodology, cyclostratigraphic and astronomical tuning analyses, writing, and funding acquisition. M.F.F.: conceptualization, methodology, and writing. C.A.P.: paleomagnetic analyses and writing. J.N.L.: biostratigraphical analysis and writing. J.K.: Sedimentological analyses and writing. P.A.S.: biostratigraphical analysis and writing. R.P.S.Jr.: Validation, investigation, project administration, and writing.

## Competing interests

The authors declare no competing interests.

## Additional information

**Supplementary information** The online version contains supplementary material available at <https://doi.org/10.1038/s43247-025-02910-0>.

**Correspondence** and requests for materials should be addressed to J. M. F. Ramos.

**Peer review information** *Communications Earth & Environment* thanks Tim van Peer, Dan Palcu and the other, anonymous, reviewer(s) for their contribution to the peer review of this work. Primary Handling Editors: Deborah Tangunan and Alireza Bahadori. A peer review file is available.

**Reprints and permissions information** is available at <http://www.nature.com/reprints>

**Publisher's note** Springer Nature remains neutral with regard to jurisdictional claims in published maps and institutional affiliations.

**Open Access** This article is licensed under a Creative Commons Attribution-NonCommercial-NoDerivatives 4.0 International License, which permits any non-commercial use, sharing, distribution and reproduction in any medium or format, as long as you give appropriate credit to the original author(s) and the source, provide a link to the Creative Commons licence, and indicate if you modified the licensed material. You do not have permission under this licence to share adapted material derived from this article or parts of it. The images or other third party material in this article are included in the article's Creative Commons licence, unless indicated otherwise in a credit line to the material. If material is not included in the article's Creative Commons licence and your intended use is not permitted by statutory regulation or exceeds the permitted use, you will need to obtain permission directly from the copyright holder. To view a copy of this licence, visit <http://creativecommons.org/licenses/by-nc-nd/4.0/>.

© The Author(s) 2025